

The interplay of insulating and superconducting orders in magic-angle graphene bilayers

Petr Stepanov¹, Ipsita Das¹, Xiaobo Lu¹, Ali Fahimniya², Kenji Watanabe³, Takashi Taniguchi³, Frank H. L. Koppens¹, Johannes Lischner⁴, Leonid Levitov² and Dmitri K. Efetov^{1*}

1. ICFO - Institut de Ciències Fòniques, The Barcelona Institute of Science and Technology, Castelldefels, Barcelona, 08860, Spain
2. Department of Physics, Massachusetts Institute of Technology, Cambridge MA 02139, USA
3. National Institute for Materials Science, 1-1 Namiki, Tsukuba, 305-0044, Japan
4. Departments of Materials and Physics and the Thomas Young Centre for Theory and Simulation of Materials, Imperial College London, London SW7 2AZ, United Kingdom

*E-mail: dmitri.efetov@icfo.eu

The recent discovery of superconducting and correlated insulating states coexisting in magic-angle twisted bilayer graphene(1-11) (MAG) at commensurate fillings have raised fascinating questions about the interplay of these orders. Tuning electron-electron interactions in MAG would shed light on the individual roles of these phases and their intricate relationship. Here we report on a new method to control electronic interactions in a correlated system, by varying the separation of a metallic screening layer in ultra-close proximity to a MAG layer(12,13). We observe that correlated insulators disappear when the separation becomes smaller than the extent of Wannier orbitals, $w < 15\text{nm}$, consistent with the expected screening of Coulomb interactions. The superconducting phase remains resilient under screening, taking over the phase space vacated by correlated insulators and showing critical temperatures comparable to those in unscreened devices. However, even under screening, correlated insulators reappear at half-filling upon applying small out-of-plane magnetic field > 0.5 tesla, exhibiting Chern bands with quantized Hall resistance of $h/2e^2$ consistent with orbital magnetism. Our study establishes direct and independent control of the insulating and superconducting phases, pointing to their possibly distinct microscopic origin. The re-examination of the often-assumed “mother-child relation” between these phases, triggered by these observations, illustrates a new technique to directly probe microscopic mechanisms of anomalous superconductivity in MAG and other strongly-correlated systems.

Strongly correlated electron systems exhibit a vast richness of different types of interactions and emergent orders. Understanding this complexity and identifying the microscopic interactions that govern specific orders is one of the great unsolved problems in condensed matter physics. Famously, the concurrence of unconventional superconductivity (SC) and correlated insulating (CI) phases in cuprates, pnictides and heavy fermion compounds(14-16), has led to the conjecture that superconductivity could be assisted by CI order, arising from a purely electronic mechanism. Achieving a direct control of electron-electron (e-e) interactions – a long-standing goal in the study of correlated electron systems – would clarify the separate origin and the complex relation between these phases. However, despite strong interest, previous attempts to control e-e interactions in other crystalline correlated systems were impeded by small atomic orbital sizes and strong sensitivity to doping(17).

Flat moiré bands in MAG(1-11) and similar systems(18-21) host strongly-correlated electrons that exhibit a variety of interesting ordered states, notably correlated insulators(1,4) (CI), superconductors(2-4) (SC), magnets and topological states(4-6). Initial experiments suggested a

connection between insulating states at integer occupancies of the moiré bands and superconducting domes appearing upon slight additional doping (2). These observations suggested that these phases could be directly related and arise from a common mechanism, similar to the scenarios that have been proposed for the cuprates(14).

The unique properties of MAG, in particular, its exceptionally large moiré superlattice unit cell, enable new methods for testing this hypothesis that are not readily available in other systems. Namely, it is possible to assemble MAG into two-dimensional van der Waals hetero-structures(23) with metallic layers that are separated from the MAG only by a ultra-thin dielectric spacer of hexagonal boron nitride (hBN). If the distance w between MAG and the metallic layers is smaller than the size of the moiré unit cell, $w < \lambda \sim 15\text{nm}$, the screening by the polarization charges induced in the metallic layers will suppress the long-range part of the Coulomb interaction. Such suppression will lead to a large reduction of the on-site Hubbard interaction U and extinction of the CI order (12,13) (Fig. 1A-B, see supplementary information for modeling details).

Here we report on a transport study of proximally screened MAG devices with controlled ultra-thin hBN spacer thickness. We find a strong suppression of CI states when graphite screening layers are placed closer than 10nm away from the MAG layers. At the same time, the superconducting states, rather than being weakened, take over the phase space vacated by the insulating states (Fig. 1C). We note that in all previous studies screening effects were negligible as metallic layers were placed $> 30\text{nm}$ away from the MAG(2,3), in which case insulators always prevail over superconductivity at integer fillings. In strongly screened devices, however, superconducting regions can span wide doping regions without being interrupted by CI states. This observation suggests that the insulating and superconducting orders - rather than sharing a common origin - actually compete with each other, in contrast to what could be expected from a simple analogy to the cuprates.

All studied devices displayed high spatial uniformity, allowing us to rule out a disorder-induced “cloaking” of the correlated insulators. This is evident from the sharpness of the charge neutrality point and the band-gap edges at complete filling of the moiré bands (Fig. 2A and supplementary information). Moreover, all devices showed very small twist-angle inhomogeneity, with variation as small as $\Delta\theta \sim 0.02^\circ$ per $20\mu\text{m}$ (SI) and robust, macroscopic superconducting states spanning the entire device area. These conclusions are confirmed by transport measurements using different contact pairs placed across the devices (Fig. 1E-F). We also rule out the possibility that the difference in the stability of the CI phases could be due to Hubbard interaction U dependence on the device-specific twist angles. Indeed, all previous studies on unscreened devices with similar twist-angles have consistently reported the existence of strongly-correlated insulators(1-11).

Fig. 1D shows an optical image of a typical transport device (D1), a quadruple vdW stack of graphite/hBN/MAG/hBN(22), where the bottom hBN layer acts as an ultra-thin $w < 15\text{nm}$ spacer between the metallic graphite and the MAG. We use four-terminal current-biased measurements to obtain the resistivity ρ_{xx} of the MAG sheet, and a gate voltage V_g on the graphite layer which allows to capacitively tune its carrier density n , which can be normalized to the band filling factor $\nu = n/n_s$ (here n_s is the full-filling electron density of the four-fold spin-valley degenerate moiré band obtained from magneto-transport measurements).

Our main findings are presented in Fig. 1C as color maps and in Fig. 2A as the corresponding line-cuts of ρ_{xx} as a function of ν and temperature T . Measurement results are shown for three representative devices with twist-angles close to the magic angle of 1.1° , but with varying ultra-

thin hBN spacer thickness. The graphs are arranged with increasing hBN thickness top to bottom, with device parameters - (D1) $w \sim 7\text{nm}$, $\theta \sim 1.15^\circ$; (D2) $w \sim 9.8\text{nm}$, $\theta \sim 1.04^\circ$ and (D3) $w \sim 12.5\text{nm}$, $\theta \sim 1.10^\circ$. Notably, the device with the thinnest hBN spacer, D1 ($w \sim 7\text{nm}$), demonstrates a phase diagram that is drastically different from all previously reported MAG devices(1–4). Strikingly, it entirely lacks CI states, with ρ_{xx} values never exceeding a few $\text{k}\Omega$ at all integer band fillings, and in particular showing clearly metallic $\rho_{xx}(T)$ behaviors at $\nu = \pm 2$ (Fig. 2B). At the same time we observe two broad SC domes in both the valence and conduction moiré bands, with the values of $T_c \approx 920\text{ mK}$ and $T_c \approx 420\text{ mK}$, respectively (Fig. 1E) (see supplementary information for full characterization of the SC states). These SC domes are not accompanied by insulating states, they span across integer fillings uninterrupted by the CI states. The observed superconducting T_c values are comparable to those reported previously for devices with similar twist-angles and in the presence of strong insulators(2, 3).

This behavior is in stark contrast to that seen in the device with the thickest hBN spacer, D3 ($w \sim 12.5\text{nm}$), which overall has the closest resemblance to previously reported devices(1–4). We find resistance peaks at all integer fillings and strong temperature activated CI states at filling of $\nu = \pm 2$ (with $\Delta \sim 0.34\text{ meV}$ (-) and $\Delta \sim 0.37\text{ meV}$ (+)) and $\nu = 3$ ($\Delta \sim 0.25\text{ meV}$) (Fig. 2A). Four SC domes directly flank the CI states with T_c values ranging from 150mK to 3K. However, at integer fillings the resistive states always persist. Sample D2 ($w \sim 9.8\text{nm}$) has an intermediate hBN spacer thickness and displays features present in both D1 and D3 devices. While the device does not display correlated insulating states in the entire valence band, it shows a single SC dome with a $T_c \approx 400\text{ mK}$. In the conduction band it features a resistance peak at $\nu = 2$, which shows a clear activated dependence vs. T , suggesting a weak, underdeveloped CI state. Flanking this state from both the hole and electron doping sides, there are two SC domes with $T_c \approx 500\text{ mK}$ and $T_c \approx 650\text{ mK}$, respectively.

We attribute the disappearance of the insulators to the Hubbard interaction U weakening due to screening by nearby graphite as well as by the widening of the flat band width for twist angles deviating from magic angle $\sim 1.1^\circ$. This is in agreement with the pronounced insulating behavior seen in device D3 despite the relatively thin hBN, as it has a twist angle of exactly 1.1° . In devices D1 and D2, featuring an even thinner hBN, the CI state is additionally weakened by the flat band widening away from the magic angle. The enhanced screening results in CIs completely disappearing. However, we rule out that the complete disappearance of CIs in D1 and D2 is solely due to twist-angle variation, as in previously reported measurements strong CIs appeared across a wide range of twist angles around magic angle 1.1° , and their absence was never reported. In that regard we also note that CI states with activation behavior have been reported in a relatively narrow range of twist angles $\theta = 1.07^\circ - 1.16^\circ$ (1–5). Taking limited data from literature, we note that typically large CI gaps were found at $\nu = \pm 2$, ranging between $0.31 - 1.3\text{ meV}$ (1,3,4). In comparison, superconductivity was seen in devices with a somewhat wider range of twist angles, between $\theta = 1.02^\circ$ to 1.16° (2).

An overall comparison among the three devices indicates that correlated insulating order is suppressed for devices where the twist-angles substantially deviate from 1.1° and the hBN spacer thickness is reduced to less than 10nm. While CIs are well developed for device D3, signatures of CIs have almost vanished in D2, and are completely absent in D1. Device D1 displays one broad SC dome per moiré valence and conduction band, where the position of the SC dome in the conduction band coincides with $\nu = 2$, spanning over it without interruption. In device D2 we observe one broad SC dome in the valence band, and two much narrower domes in the conduction band around $\nu = 2$ filling, which are separated by an emerging CI. These findings suggest that CIs may interrupt a broader SC dome and split it in two(24,25). At the

same time, SC domes do not seem to coincide with the $\nu = \pm 2$ positions, but are broadly dispersed across the moiré bands. It remains also unclear whether their positions coincide with the van Hove singularities (vHs) of the interaction reconstructed flat bands, as Hall measurements (supplementary information) cannot conclusively identify their position, due to coinciding SC domes at low magnetic fields, and developing interaction gaps at higher fields(24-28).

However, the strongly-correlated behavior persists even in the absence of CIs, as demonstrated by transport properties of device D1 in a perpendicular magnetic field B . We observe that at field as low as $B > 0.3\text{T}$ a correlated insulating phase develops at the $\nu = -2$ filling, which is evident by a transition from a metallic to an activated transport behavior (Fig. 3A). Fitting $R_{xx} \sim \exp(\Delta/2kT)$ as a function of B (right panel Fig. 3A), shows an approximately linear evolution of Δ . We attribute this effect to field-induced quenching of the electron dynamics, where the magnetic field "freezes" the kinetic energy of the electrons by creating Aharonov-Bohm flux through each moiré super-cell(29-30). This effect tips the balance between the kinetic energy and Coulomb interaction in favor of the latter, leading to the reappearance of the CI.

Strikingly, the reappearing CI order is accompanied by a quantized Hall state, which occurs at a slightly lower density. At fields as low as $B > 0.4\text{T}$ we observe regions of near-perfectly quantized plateaus of Hall resistance $R_{xy} \sim h/2e^2 = 12.9 \text{ k}\Omega$ (with e the electron charge and h Planck's constant), accompanied by a vanishing longitudinal resistance $R_{xx} \sim 0 \Omega$. These values are consistent with the degeneracy of the expected CI at half-filling(1) and are two times smaller than the free-electron values. Starting from $\nu = -2$ filling at $B = 0$, these states form in very broad regions in the n - B phase space, spanning into larger densities as B increases, following an $dn/dB = 2e/h$ dependence, which is consistent with a Chern number of $C = 2$.

The magnetic field required to induce this quantized Hall state is considerably lower than the fields at which Landau levels are seen, $B > 3\text{T}$. We therefore conclude that this quantized state originates from electron-electron interactions rather than the single-particle effects. Theory predicts that strong correlations can favor a valley-polarized Chern insulator even for untwisted bilayer graphene(32-34), however in topological moiré flat-bands in MAG correlations are expected to boost and strengthen the Chern insulator order. Similar observations were made recently in hBN aligned(5-6) and non-aligned MAG(4) and in ABC trilayer graphene(19-20) for odd integer filled states, where orbital magnetic states were observed. While at $B = 0\text{T}$ we do not observe signatures of hysteresis with the B -field sweeping direction, sizeable hysteresis appears around $B \sim 0.5\text{T}$, signaling the existence of similar orbital magnetic states(25).

What are the implications of these findings for the origin of the superconducting state? The observed resilience of superconductivity upon suppression of the insulating phase is consistent with the two phases competing rather than being intimately connected. Such competition would be hard to reconcile with a common microscopic mechanism of the two phases suggested by an analogy with cuprates. One explanation could be that Coulomb interactions drive the formation of the commensurate insulators while superconductivity arises from a more conventional mechanism. However, the anomalous character of superconductivity in MAG, occurring at record-low carrier densities, suggests that the electron-phonon mechanism, if present, is enhanced by the high density of states and, possibly, assisted by Coulomb interactions. The reappearance of correlated insulator phases in small magnetic field confirms that correlations remain very strong in the system, suggesting that an exotic mechanism for the superconducting order, potentially involving a correlated-metal parent states, is indeed highly likely.

References

1. Y. Cao, V. Fatemi, A. Demir, S. Fang, S. L. Tomarken, J. Y. Luo, J. D. Sanchez-Yamagishi, K. Watanabe, T. Taniguchi, E. Kaxiras, R. C. Ashoori, P. Jarillo-Herrero, Correlated insulator behaviour at half-filling in magic-angle graphene superlattices. *Nature*. **556**, 80–84 (2018).
2. Y. Cao, V. Fatemi, S. Fang, K. Watanabe, T. Taniguchi, E. Kaxiras, P. Jarillo-Herrero, Unconventional superconductivity in magic-angle graphene superlattices. *Nature*. **556**, 43–50 (2018).
3. M. Yankowitz, S. Chen, H. Polshyn, Y. Zhang, K. Watanabe, T. Taniguchi, D. Graf, A. F. Young, C. R. Dean, Tuning superconductivity in twisted bilayer graphene. *Science* **363**, 1059–1064 (2019).
4. X. Lu, P. Stepanov, W. Yang, M. Xie, M. A. Aamir, I. Das, C. Urgell, K. Watanabe, T. Taniguchi, G. Zhang, A. Bachtold, A. H. MacDonald, D. K. Efetov, Superconductors, Orbital Magnets, and Correlated States in Magic Angle Bilayer Graphene. *Nature*. **574**, 653–657 (2019).
5. M. Serlin, C. L. Tschirhart, H. Polshyn, Y. Zhang, J. Zhu, K. Watanabe, T. Taniguchi, L. Balents, A. F. Young, Intrinsic quantized anomalous Hall effect in a moiré heterostructure, arXiv:1907.00261 (2019).
6. A. L. Sharpe, E. J. Fox, A. W. Barnard, J. Finney, K. Watanabe, T. Taniguchi, M. A. Kastner, D. Goldhaber-Gordon, Emergent ferromagnetism near three-quarters filling in twisted bilayer graphene, *Science* **365**, 605–608 (2019).
7. Yonglong Xie, Biao Lian, Berthold Jäck, Xiaomeng Liu, Cheng-Li Chiu, Kenji Watanabe, Takashi Taniguchi, B. Andrei Bernevig & Ali Yazdani, Spectroscopic signatures of many-body correlations in magic-angle twisted bilayer graphene, *Nature* **572**, 101 (2019).
8. Alexander Kerelsky, Leo J. McGilly, Dante M. Kennes, Lede Xian, Matthew Yankowitz, Shaowen Chen, K. Watanabe, T. Taniguchi, James Hone, Cory Dean, Angel Rubio & Abhay N. Pasupathy, Maximized electron interactions at the magic angle in twisted bilayer graphene, *Nature* **572**, 95–100 (2019).
9. Yuhang Jiang, Xinyuan Lai, Kenji Watanabe, Takashi Taniguchi, Kristjan Haule, Jinhai Mao & Eva Y. Andrei, Charge order and broken rotational symmetry in magic-angle twisted bilayer graphene, *Nature* **573**, 91–95 (2019).
10. Youngjoon Choi, Jeannette Kemmer, Yang Peng, Alex Thomson, Harpreet Arora, Robert Pol-ski, Yiran Zhang, Hechen Ren, Jason Alicea, Gil Refael, Felix von Oppen, Kenji Watanabe, Takashi Taniguchi & Stevan Nadj-Perge, Electronic correlations in twisted bilayer graphene near the magic angle, *Nature Physics* **15**, 1174–1180 (2019).
11. Aviram Uri, Sameer Grover, Yuan Cao, JA Crosse, Kousik Bagani, Daniel Rodan-Legrain, Yuri Myasoedov, Kenji Watanabe, Takashi Taniguchi, Pilkyung Moon, Mikito Koshino, Pablo Jarillo-Herrero, Eli Zeldov, Mapping the twist angle and unconventional Landau levels in magic angle graphene, arXiv:1908.04595 (2019).
12. Z. A. H. Goodwin, F. Corsetti, A. A. Mostofi, J. Lischner, Twist-angle dependence of electron correlations in moiré graphene bilayers. *Phys. Rev. B*. **100**, 121106 (2019).
13. J. M. Pizarro, M. Rösner, R. Thomale, R. Valentí, T. O. Wehling, Internal screening and dielectric engineering in magic-angle twisted bilayer graphene. *Phys. Rev. B*. **100**, 161102 (2019).
14. Patrick A. Lee, Naoto Nagaosa, and Xiao-Gang Wen, Doping a Mott insulator: Physics of high-temperature superconductivity, *Rev. Mod. Phys.* **78**, 17 (2006).
15. Q. Si, R. Yu, E. Abrahams, High-temperature superconductivity in iron pnictides and chalcogenides. *Nat. Rev. Mater.* **1**, 16017 (2016).
16. D. N. Basov & Andrey V. Chubukov, Manifesto for a higher T_c , *Nature Physics* **7**, 272 (2011).
17. F. Nilsson, K. Karlsson, and F. Aryasetiawan, Dynamically screened Coulomb interaction in the parent compounds of hole-doped cuprates: Trends and exceptions, *Phys. Rev. B* **99**, 075135 (2019).
18. G. W. Burg, J. Zhu, T. Taniguchi, K. Watanabe, A. H. MacDonald, E. Tutuc, Correlated Insulating States in Twisted Double Bilayer Graphene. *Phys. Rev. Lett.* **123**, 197702 (2019).
19. G. Chen, L. Jiang, S. Wu, B. Lyu, H. Li, B. L. Chittari, K. Watanabe, T. Taniguchi, Z. Shi, J. Jung, Y. Zhang, F. Wang, Evidence of a gate-tunable Mott insulator in a trilayer graphene moiré superlattice. *Nat. Phys.* **15**, 237–241 (2019).

20. Guorui Chen, Aaron L. Sharpe, Eli J. Fox, Ya-Hui Zhang, Shaoxin Wang, Lili Jiang, Bosai Lyu, Hongyuan Li, Kenji Watanabe, Takashi Taniguchi, Zhiwen Shi, T. Senthil, David Goldhaber-Gordon, Yuanbo Zhang, Feng Wang, Tunable Correlated Chern Insulator and Ferromagnetism in Trilayer Graphene/Boron Nitride Moiré Superlattice, *arXiv:1905.06535* (2019).
21. X. Liu, Z. Hao, E. Khalaf, J. Y. Lee, K. Watanabe, T. Taniguchi, A. Vishwanath, P. Kim, Spin-polarized Correlated Insulator and Superconductor in Twisted Double Bilayer Graphene (2019) (available at <http://arxiv.org/abs/1903.08130>).
22. K. Kim, A. DaSilva, S. Huang, B. Fallahazad, S. Larentis, T. Taniguchi, K. Watanabe, B. J. LeRoy, A. H. MacDonald, E. Tutuc, Tunable moiré bands and strong correlations in small-twist-angle bilayer graphene. *Proc. Natl. Acad. Sci.* **114**, 3364–3369 (2017).
23. A. K. Geim, I. V. Grigorieva, Van der Waals heterostructures. *Nature*. **499** (2013), pp. 419–425.
24. M. Ochi, M. Koshino, K. Kuroki, Possible correlated insulating states in magic-angle twisted bilayer graphene under strongly competing interactions, *Phys. Rev. B*. **98**, 081102 (2018).
25. M. Xie, A. H. MacDonald, On the nature of the correlated insulator states in twisted bilayer graphene, *arXiv:1812.04213* (2018).
26. J. F. Dodaro, S. A. Kivelson, Y. Schattner, X. Q. Sun, C. Wang, Phases of a phenomenological model of twisted bilayer graphene. *Phys. Rev. B*. **98**, 075154 (2018).
27. H. C. Po, L. Zou, T. Senthil, A. Vishwanath, Faithful tight-binding models and fragile topology of magic-angle bilayer graphene. *Phys. Rev. B*. **99**, 195455 (2019).
28. L. Zou, H. C. Po, A. Vishwanath, T. Senthil, Band structure of twisted bilayer graphene: Emergent symmetries, commensurate approximants, and Wannier obstructions. *Phys. Rev. B*. **98**, 085435 (2018).
29. C. R. Dean, L. Wang, P. Maher, C. Forsythe, F. Ghahari, Y. Gao, J. Katoch, M. Ishigami, P. Moon, M. Koshino, T. Taniguchi, K. Watanabe, K. L. Shepard, J. Hone & P. Kim, Hofstadter’s butterfly and the fractal quantum Hall effect in moiré superlattices, *Nature* **497**, 598–602 (2013).
30. B. Hunt, J. D. Sanchez-Yamagishi, A. F. Young, M. Yankowitz, B. J. LeRoy, K. Watanabe, T. Taniguchi, P. Moon, M. Koshino, P. Jarillo-Herrero, R. C. Ashoori, Massive Dirac Fermions and Hofstadter Butterfly in a van der Waals Heterostructure, *Science* **340**, 6139 (2013).
31. L. A. Ponomarenko, R. V. Gorbachev, G. L. Yu, D. C. Elias, R. Jalil, A. A. Patel, A. Mishchenko, A. S. Mayorov, C. R. Woods, J. R. Wallbank, M. Mucha-Kruczynski, B. A. Piot, M. Potemski, I. V. Grigorieva, K. S. Novoselov, F. Guinea, V. I. Fal’ko & A. K. Geim, Cloning of Dirac fermions in graphene superlattices, *Nature* **497**, 594–597 (2013).
32. R. Nandkishore, L. Levitov, Dynamical screening and excitonic instability in bilayer graphene. *Phys. Rev. Lett.* **104**, 156803 (2010).
33. R. Nandkishore, L. Levitov, Quantum anomalous Hall state in bilayer graphene. *Phys. Rev. B* **82**, 115124 (2010).
34. R. T. Weitz, M. T. Allen, B. E. Feldman, J. Martin, A. Yacoby, Broken-Symmetry States in Doubly Gated Suspended Bilayer Graphene, *Science* **330**, 812 (2010).

Acknowledgements:

We are grateful for fruitful discussions with Pablo Jarillo-Herrero, Allan MacDonald, Andrea Young, Andrei Bernevig, Biao Lian, Cory Dean. D.K.E. acknowledges support from the Ministry of Economy and Competitiveness of Spain through the “Severo Ochoa” program for Centres of Excellence in R&D (SE5-0522), Fundació Privada Cellex, Fundació Privada Mir-Puig, the Generalitat de Catalunya through the CERCA program, the H2020 Programme under grant agreement n° 820378, Project: 2D·SIPC and the La Caixa Foundation. L.L. acknowledges support from the Science and Technology Center for Integrated Quantum Materials, NSF Grant No. DMR-1231319; and Army Research Office Grant W911NF-18-1-0116. F.H.L.K. acknowledges support from the ERC consolidator grant TOPONANOP (grant agreement n° 726001). K.W. and T.T. acknowledge support from the Elemental Strategy Initiative conducted by the MEXT, Japan and the CREST (JPMJCR15F3), JST.

Author contributions:

D.K.E, P.S. and X.L. conceived and designed the experiments; P.S., X.L. and I.D. performed the experiments; P.S. and D.K.E. analyzed the data; A.F. and L.L. performed the theoretical modeling; T.T. and K.W. contributed materials; D.K.E. and F. H.L.K. supported the experiments; P.S., D.K.E and L.L. wrote the paper.

Competing financial and non-financial interests:

The authors declare no competing financial and non-financial interests.

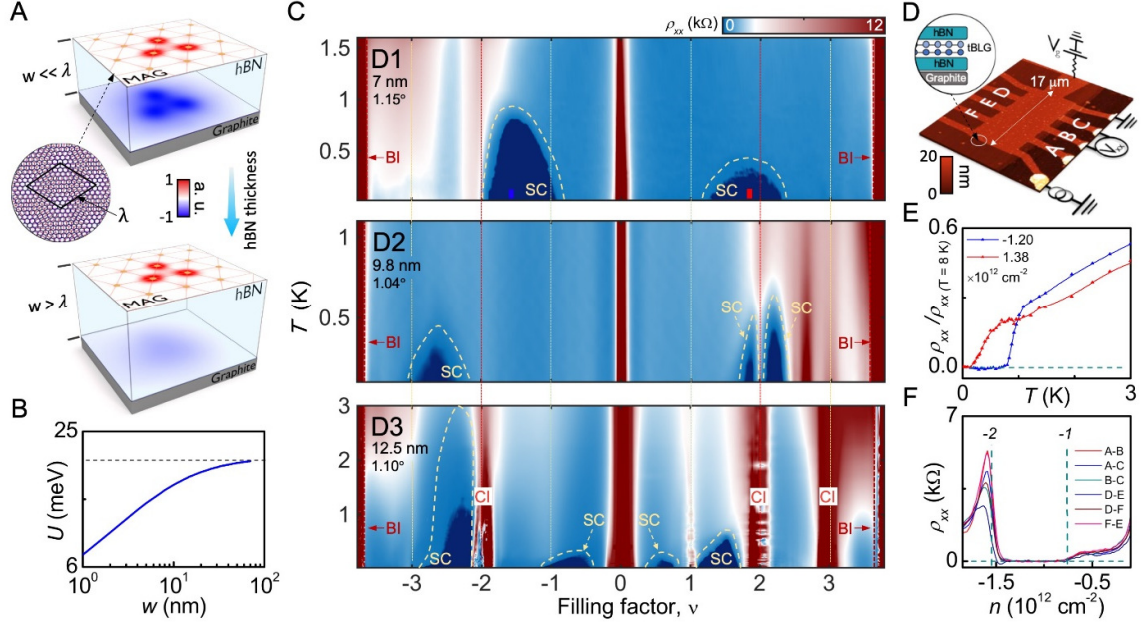


Fig. 1. Effect of screening on SC and CI phases. (A) Schematics of electronic screening of MAG. Wannier orbitals (red) in the MAG are screened by image charges on the graphite surface (blue), as calculated from (SI). (B) Hubbard interaction strength U as a function of the hBN spacer thickness w . Black dashed line marks the unscreened value. (C) Longitudinal resistivity ρ_{xx} as a function of total back-gate-induced carrier density (normalized to superlattice filling factor ν) and the device temperature T for three samples: D1 (top panel), D2 (middle panel), D3 (lower panel). Panels are arranged from the thinnest (top) to thickest (bottom) hBN spacer thickness. Experimental parameters are shown in the top left corners of the panels. Signatures of CIs are completely absent in D1, while the device exhibits superconductivity in a wide range of charge carrier densities. (D) AFM micrograph of D1. The sample demonstrates overall high structural homogeneity over a wide area: 17 μm long and 6 μm wide. MAG is fully encapsulated between hBN sheets. A graphite flake underneath the stack acts as a back gate. (E) Thermal activation of SC in D1. Resistivity (normalized to high temperature values at 8K) as a function of temperature for both SC pockets in top panel in (C). Line cuts are taken at charge carrier densities marked by red and blue rectangles in (C). (F) Four-terminal resistivity measurements vs. carrier density across pairs of contacts labeled in (D). SC persists across all contacts and shows homogeneous distribution within the same doping range.

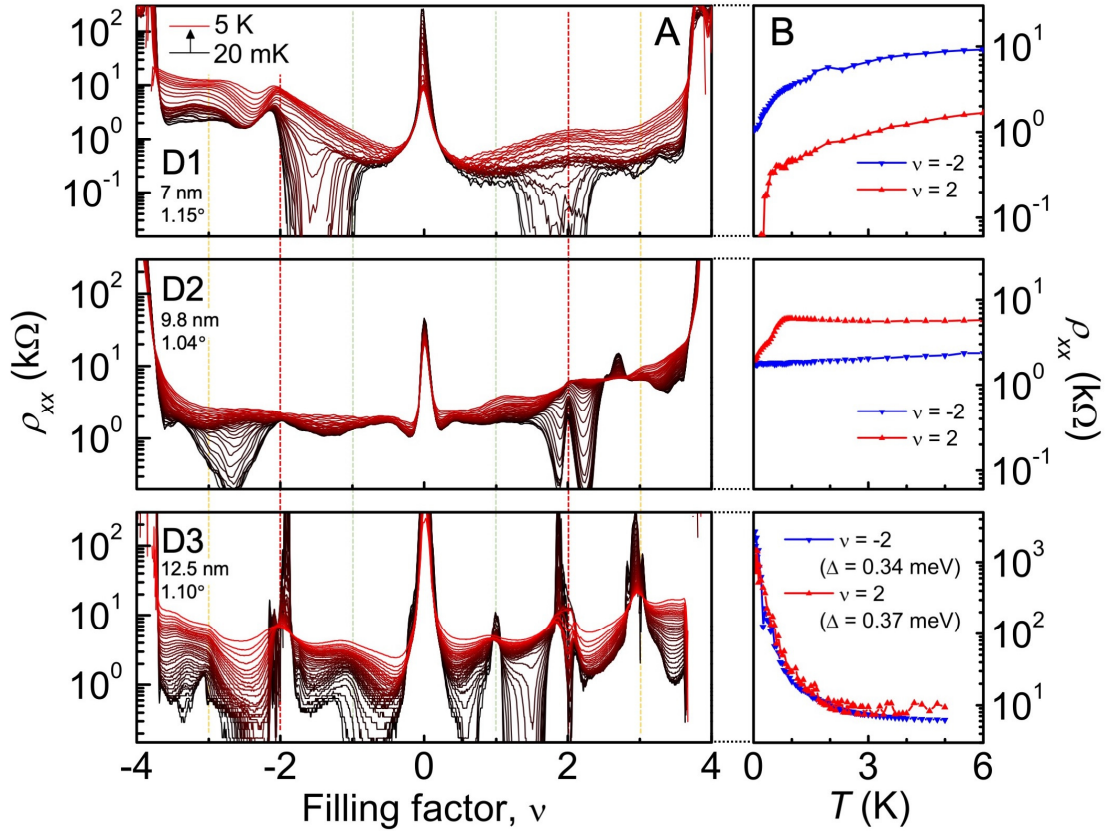


Fig. 2. **Temperature dependence in various phases across the phase diagram.** (A) Longitudinal resistivity ρ_{xx} versus carrier density (normalized to superlattice filling factor ν) taken from phase diagrams in Fig. 1D for all three devices, shown for base temperatures between 20 mK and 5 K. Panels are arranged in the same way as in Fig. 1D, illustrating the reoccurrence of CI states under increasing hBN spacer thickness. (B) Longitudinal resistivity ρ_{xx} as a function of temperature. Device D1 (top panel) shows strongly metallic behavior in both valence and conduction bands at $\nu = \pm 2$. D2 (middle panel) shows a flatter resistivity response with a small insulator activation signature in the conductance band at $\nu = +2$. D3 shows strongly developed CIs in both valence and conduction bands at $\nu = \pm 2, +1,$ and $+3$ reaching the values on the order of several $M\Omega$, consistent with a weaker interaction screening in the sample with the thickest hBN spacer.

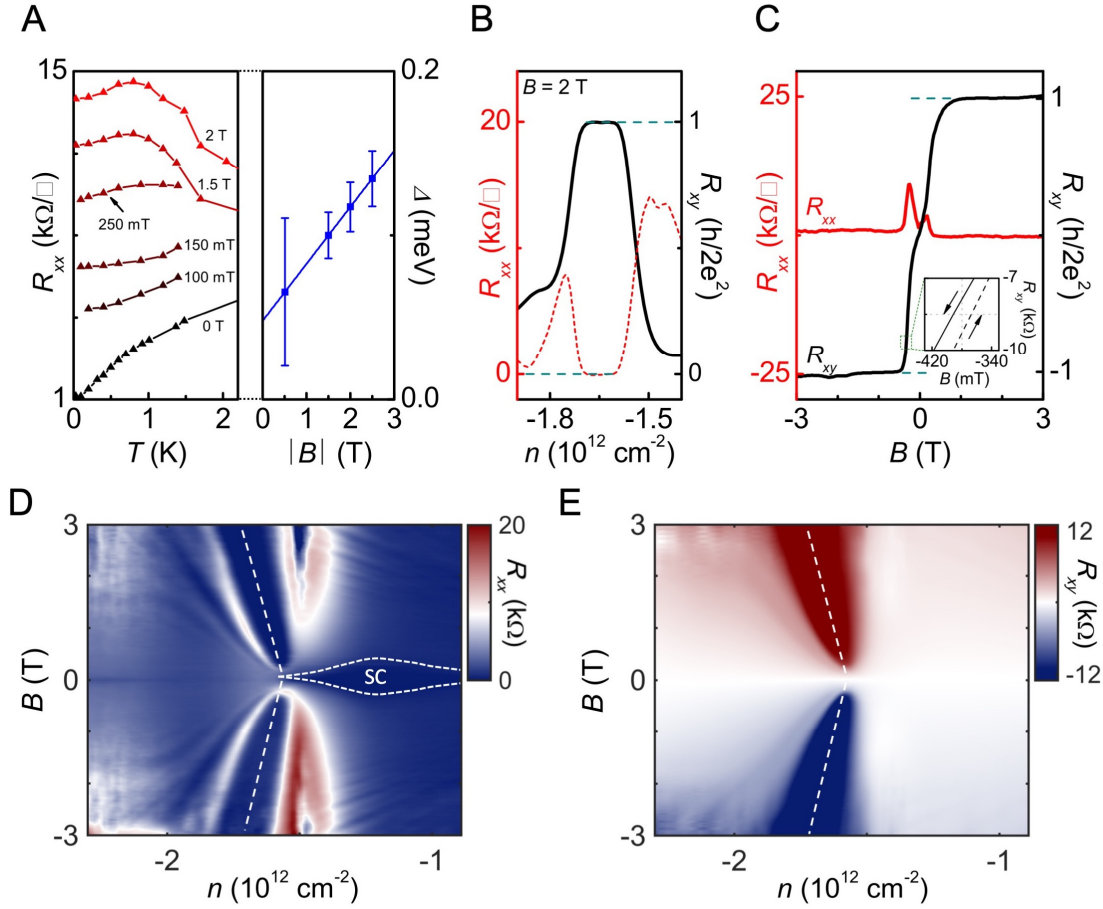


Fig. 3. Revival of the insulating phase in magnetic field. Effect of magnetic field on screened insulating phases. (A) Left panel shows longitudinal sheet resistance R_{xx} vs. device temperature T under application of finite B -fields at $\nu = -2$. The right panel shows insulator gap size estimations Δ as a function of magnetic field B . (B) Longitudinal sheet (R_{xx}) and transverse (R_{xy}) resistances as a function of charge carrier density around the quantized plateau $2e^2/h$ taken at $B = 2 \text{ T}$. (C) Longitudinal sheet resistance (red) and transverse resistance (black) vs. magnetic field B . A fully quantized plateau appears at $|B| \gtrsim 0.5 \text{ T}$. (D) Longitudinal and (E) transverse resistances versus charge carrier density and magnetic field B in the zoomed-in range of densities demonstrate the developing plateau and resistive state close to $\nu = -2$.

Supplementary Information

Methods.

Our samples in this study are fabricated using a well-established “tear-and-stack” method(1–4). Typically, a thin hBN flake is picked up by a propylene carbonate (PC) film, which is placed on a polydimethyl siloxane (PDMS) stamp at 90 °C. The hBN flake is then used to pick up a part of a monolayer graphene flake, mechanically exfoliated on Si⁺⁺/SiO₂ (285 nm) surface. Subsequently, the second half of graphene sheet is rotated to a target angle usually around $\theta \approx 1.1^\circ - 1.15^\circ$ and then picked up by hBN/graphene stack on PC from the previous step. During the next step, the heterostructure is placed on top of another thin hBN flake, that serves as a dielectric spacer. Usually, bottom hBN flake thickness is chosen by optical contrast and further confirmed with atomic force microscopy (AFM) measurements. The very bottom layer of the heterostructure consists of a relatively thick graphite flake (typically a few layer graphene > 1nm thick) that acts as a local back gate. The final stack is then placed on Si/SiO₂ (285 nm) wafer, where it is further etched into a multiple Hall bar geometry using CHF₃/O₂ plasma and coupled to Cr/Au (5/50 nm) metal contacts(5).

Dielectric thickness measurements.

Bottom hBN thickness is extracted from AFM data. Fig. S1 demonstrates a set of MAG heterostructures that has been used to fabricate devices in the main text. The upper panel of Fig. S1 shows an optical image of the final hBN/MAG/hBN/graphite stack. We find that the heterostructures exhibit high structural homogeneity with visible absence of trapped air bubbles, known to distort twist angle and charge carrier density locally(6). This observation is further confirmed by the AFM scans shown on the insets. The AFM scans are also used to extract the topography of the fabricated stacks and find the bottom hBN thicknesses $h = 7$ nm (D1), 9.8 nm (D2) and 12.5 nm (D3).

The difference in bottom dielectric thickness is further confirmed by measurements of the capacitance between graphite gate and MAG. Extracted from the SdH oscillations map (exampled in Fig. S6), we find that capacitance changes from 355nf/cm² (D1) to 260nf/cm² (D2) and further to 221 nf/cm² (D3). Thus, the back gate capacitance increases by ~60%, compared between devices D3 and D1 in a good agreement with AFM height profile measurements.

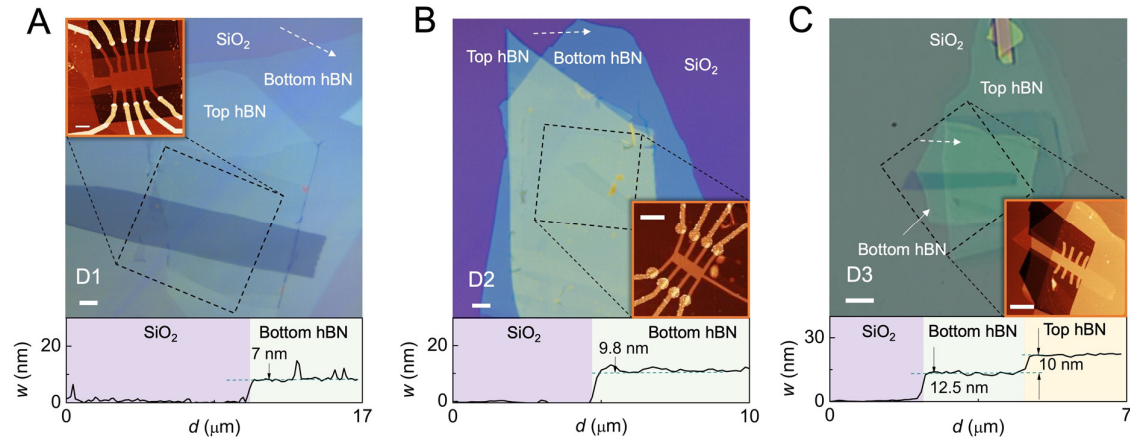


Fig. S1. **AFM and optical micrographs for samples D1(A), D2(B), and D3(C) reported in the main text.** The main panels are optical images of final stacks, from which all three devices were fabricated. The insets demonstrate AFM scans of the final devices etched into multi-terminal Hall bar geometries. Dashed black squares show AFM image areas. Bottom hBN thickness measurements are shown on the lower panel graphs. Height profiles are taken along the white dashed arrow lines. Scale bars are 5 μm .

Effect of disorder.

During stacking of graphene parts twist angle disorder may be introduced into the final heterostructure. To further analyze sample's twist angle homogeneity, we perform two-terminal conductance measurements with subsequent check for global twist angle values between different sets of contact pairs. Fig. S2 shows two-terminal conductance as a function of charge carrier density for device D1. The sample has ten contacts, out of which thirteen two-terminal conductance datasets have been obtained along and across the sample bulk. Contact pairs on the right-hand side of the sample (A-B, B-C, C-D, and D-E) demonstrate the highest angle homogeneity with maximum charge carrier density deviation of the full filled superlattice unit cell $\delta n_s^{max} \approx 0.03 \times 10^{12} \text{ cm}^{-2}$. Among them, contact pair C-D has been used to obtain longitudinal resistance data R_{xx} in this device. Overall, the graph demonstrates high global twist angle homogeneity as the positions of band-insulator regions match exceptionally well with maximum charge carrier density deviation across all contact pairs $\delta n_s^{max} \approx 0.18 \times 10^{12} \text{ cm}^{-2}$. We also note that the position of CNP remains almost intact in absolute back gate voltage values for each of the pair ($V_g^{CNP} = -4 \pm 1 \text{ mV}$).

In addition, we perform analysis on the full width at half of maximum resistance (FWHM) at CNP. We estimate charge carrier inhomogeneity $\delta n \approx 1.8 \times 10^{10} \text{ cm}^{-2}$. This measurement suggests that the inhomogeneity on the right-hand side of the sample is mainly defined by the charge disorder. Here we note that a percolating superconducting network can short circuit the insulating phase at $\nu = \pm 2$. However, the exceptionally low level of the charge inhomogeneity in combination with low-twist angle disorder cannot sufficiently explain a possible mixing between resistive and superconducting phases in the light of a complete absence of resistive states on both electron and hole-doped flat-bands of the studied devices.

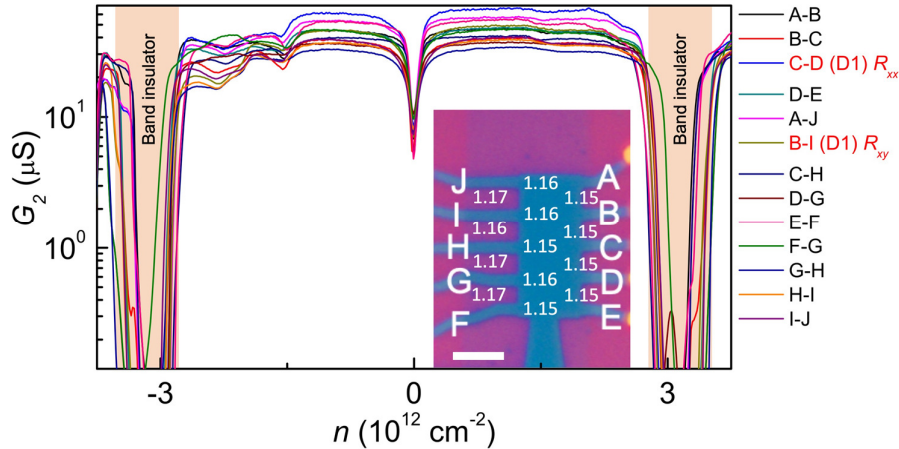


Fig. S2. **Two-terminal conductance measurements across all available contacts in device D1.** The legend shows contact pairs corresponding to the inset optical image of the device. The numbers on the device optical micrograph correspond to measured global twist angle values between contact pairs (extracted from resistance maxima). Scale bar is 5 μm .

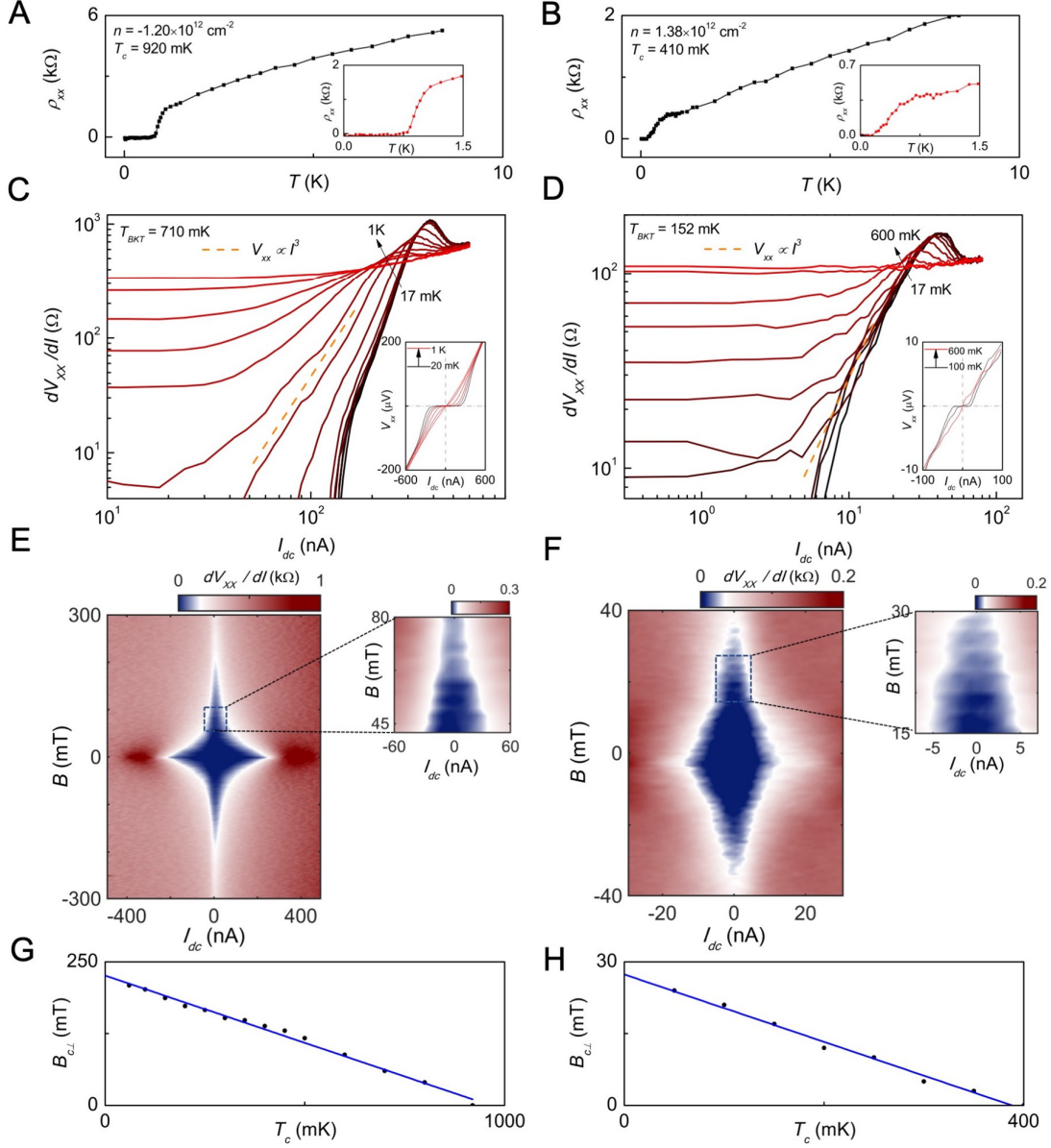


Fig. S3. **SC states characterization in device D1.** The right- (left-) hand side of the figure refers to SC pocket in the valence (conductance) band on the top panel of Fig. 1C in the main text. (A-B) Temperature activation of superconductivity for both pockets on the absolute resistance scale. The insets demonstrate a zoomed-in range of temperatures from 0 K to 1.5 K. (C-D) Berezinskii-Kosterlitz-Thouless (BKT) measurements of differential resistance dV_{xx}/dI versus DC current bias I_{dc} for both SC pockets. The insets show DC voltage as a function DC current bias taken at different temperatures for optimally doped SC states. (E-F) Differential conductance dV_{xx}/dI (color) as a function of perpendicular magnetic field B and DC current bias I_{dc} shows distinct diamond-like features for both pockets. Zoomed-in images (to the right) show clear Fraunhofer interference patterns, which are a solid proof of superconductivity. (G-H) Ginzburg-Landau coherence length measurements for both pockets. Critical field $B_{c\perp}$ versus critical temperature T_c taken at half of normal state resistance values. Black dots refer to experimentally obtained values, blue lines are linear fit to the data. We estimate coherence length $\xi_{GL} = 38 \text{ nm}$ (g) and $\xi_{GL} = 101 \text{ nm}$ (h).

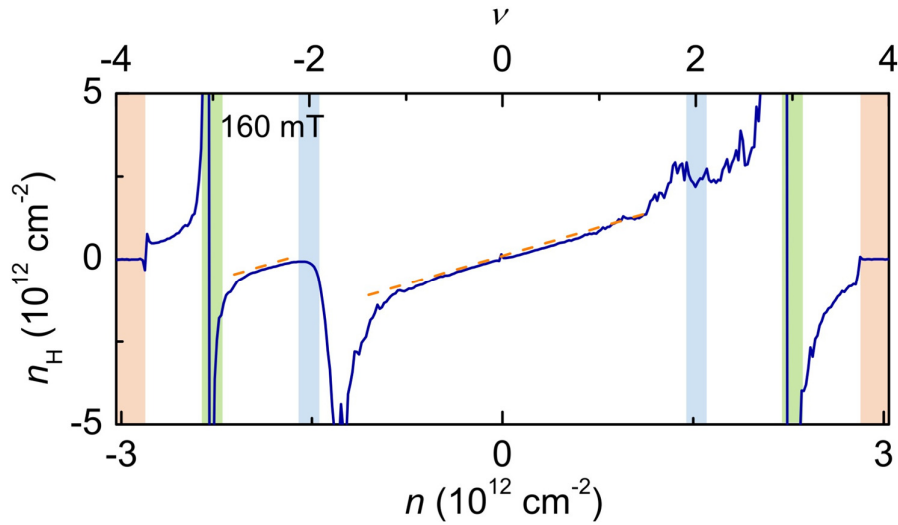


Fig. S4. **Hall density measurements in device D1.** Hall density n_H versus charge carrier density n extracted from the low-field Hall resistance measurements at 160 mT.

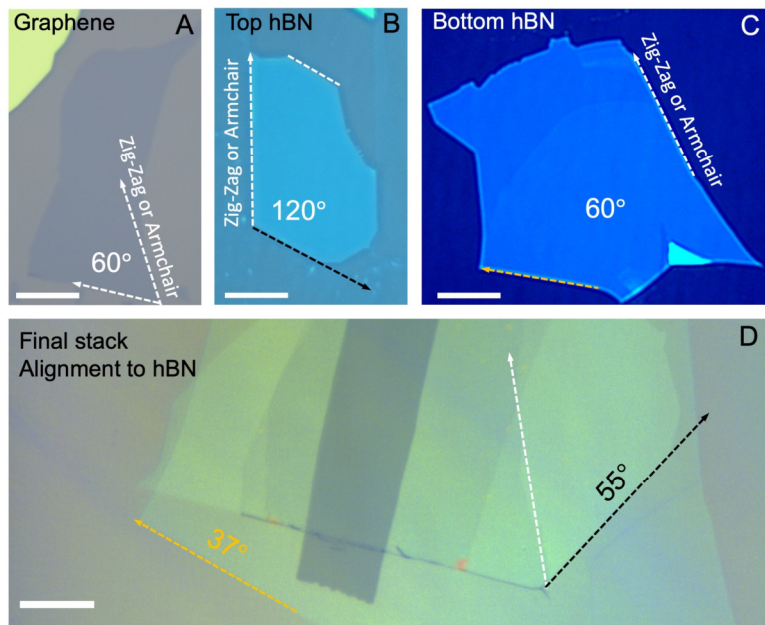


Fig. S5. **Check for alignment to hBN.** (A) Optical image of the monolayer graphene flake on SiO_2 substrate used for fabrication of MAG heterostructure. White dashed arrows indicate preferable lattice directions (zig-zag or armchair). (B) Optical image of the top hBN flake. (C) Optical micrograph of the bottom hBN flake. (D) Optical image of the final stack on SiO_2 substrate. Black dashed arrow indicates the edge of top hBN shown in (B). Orange dashed arrow corresponds to the edge of the bottom hBN shown in panel (C). Black (orange) numbers correspond to angle between white dashed arrow (graphene edge) and top (bottom) hBN. We estimate twist angle between bottom hBN and MAG $\approx 7 (\pm 1.5)^\circ$ or $\approx 23 (\pm 1.5)^\circ$ and between top hBN and MAG $\approx 25 (\pm 1.5)^\circ$ or $\approx 5 (\pm 1.5)^\circ$. Furthermore, we don't find signatures of alignment to hBN in magnetic field SdH oscillation data for neither of three devices (e.g. Fig. S6). Scale bars are 20 μm .

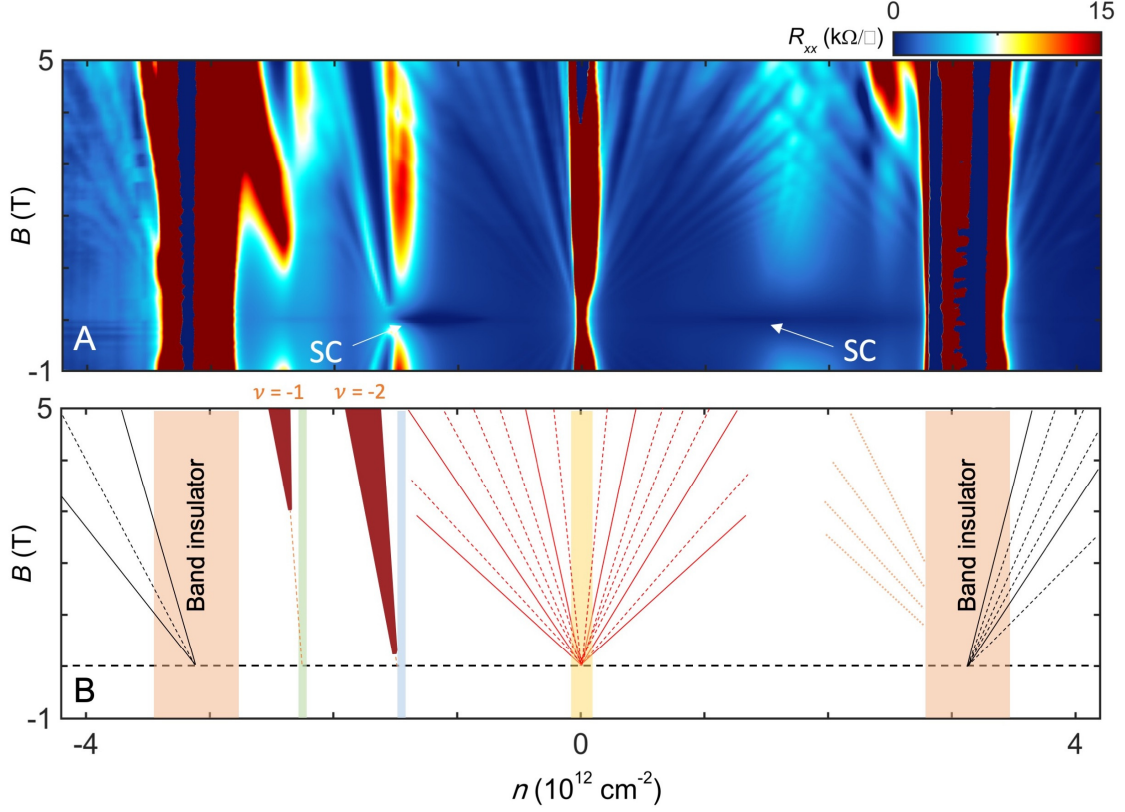


Fig. S6. **Full range magnetic field phase diagram in device D1.** (A) Longitudinal sheet resistance R_{xx} (color) versus change carrier density n and perpendicular magnetic field B . (B) Schematic image of Landau levels shown in (A). Solid lines correspond to 4-fold degenerate levels with quantized plateaus $\nu_{LL} = 4, 8, 12, \dots$. Dashed lines show broken spin or/and valley degeneracy levels. Dark red features to the left show Chern insulator states originating from $\nu = -2$ (-3)-filled superlattice unit cell corresponding to quantization of $\frac{2e^2}{h}$ ($\frac{e^2}{h}$). Blue and green transparent stripes on the left side of the graph correspond to superlattice unit cell with fillings $\nu = -2$ and -3 , respectively.

The phase diagram shown on the Fig. S6A is also used to make estimation for the twist angle in the studied devices. We use the relation $n_s/\nu \approx \frac{2\theta^2}{\sqrt{3}a^2}$, where $a = 0.246$ nm is the lattice constant of graphene and n_s is the charge carrier density corresponding to full filled superlattice unit cell. SdH oscillations propagating outside of the full filled flat band (e.g. black solid and dashed lines in Fig. S6B) converge at a point on the x -axis that defines n_s . Using that, we find $n_s = 3.04 \times 10^{12} \text{ cm}^{-2}$ (or in the absolute gate voltage values $V_g - V_g^{CNP} = 1.38$ V). This constitutes the twist angle in D1 $\theta \approx 1.15^\circ$.

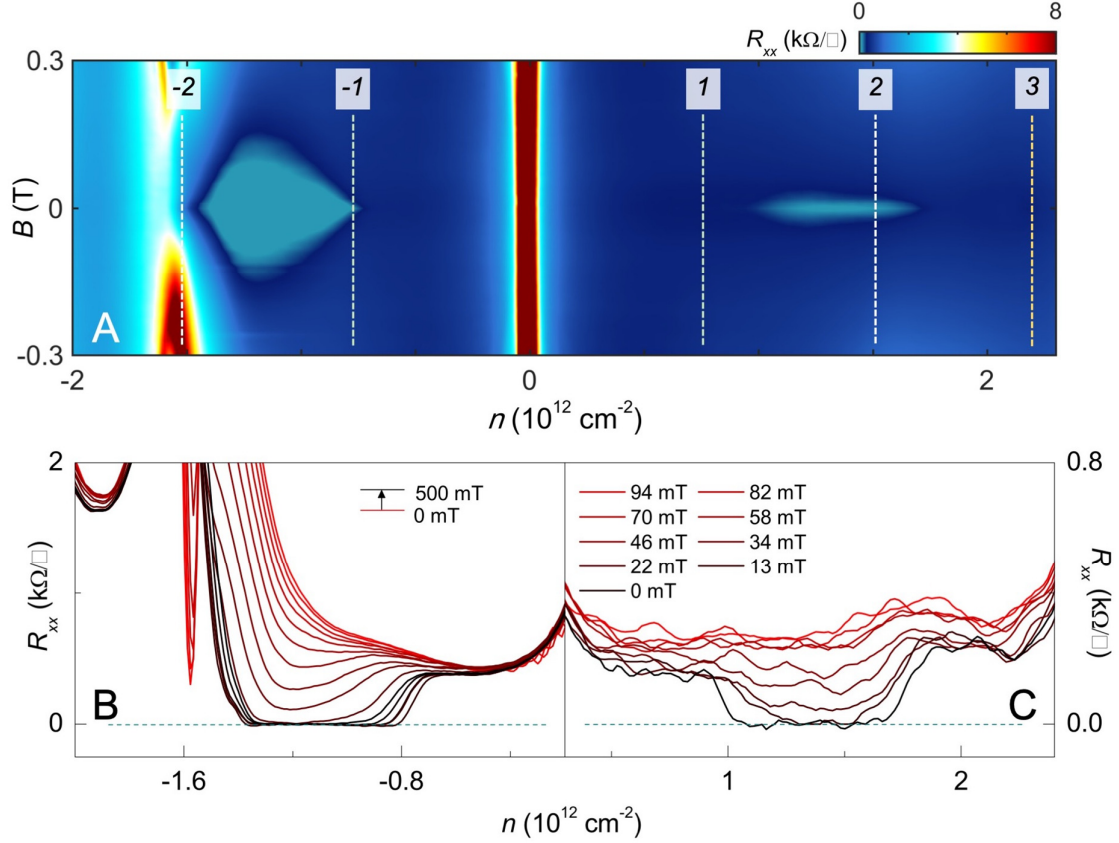


Fig. S7. **Effect of low magnetic field on correlated states in device D1.** (A) Longitudinal sheet resistance R_{xx} (color) versus change carrier density n and perpendicular magnetic field B . (B) R_{xx} as a function of charge carrier density n for valence band SC pockets in (A). (C) Resistance versus charge carrier density for valence band SC pockets in (A).

Modeling Screening of Coulomb interactions in MAG/hBN/graphite heterostructures

Here we discuss the model used to describe screening in MAG/hBN/graphite heterostructure. There are three different mechanisms that contribute to electric polarization responsible for screening. One is due to the intrinsic (interband and intraband) polarizability of MAG itself, the other is due to the dielectric permittivity of hBN, and the third one is due to image charges on the surface of the graphite gate. In that, we will treat the graphite gate as an ideal conductor, setting electrostatic potential equal zero on the graphite surface. The ideal conductor approximation is justified because the typical screening length in graphite (~ 1 nm) is much smaller than the hBN spacer thicknesses used in studied devices.

We consider the MAG layer positioned at $z = 0$ and the hBN spacer of width w located at $-w \leq z \leq 0$. We then expand the potential of a point charge positioned in MAG plane, $\phi(\mathbf{r}, z)$, as a sum of Fourier harmonics varying in constant- z planes with coefficients that depend on z ,

$$\phi(\mathbf{r}, z) = \sum_q \phi_q(z) e^{iq \cdot \mathbf{r}}$$

Poisson's equation, written in terms of the quantities $\phi_q(z)$, reads

$$(\partial_z \kappa(z) \partial_z - \kappa(z) q^2) \phi_q(z) = -4\pi(e + \phi_q(z) \Pi_q) \delta(z)$$

Here, $\kappa(z)$ is the dielectric permittivity of hBN, taken to be $\kappa_{\text{hBN}} \approx 3.5$ for $-w \leq z \leq 0$ and 1 otherwise, and Π_q denotes the intrinsic polarizability of MAG.

Solving Poisson's equation for $\phi_q(z=0)$ with the ideal conductor boundary condition on the graphite surface, $\phi_q(z=-w) = 0$, yields

$$\phi_q(z=0) = \frac{4\pi e}{q(1 + \kappa_{\text{hBN}} \coth qw) - 4\pi \Pi_q}$$

For a numerical estimate, we approximate the polarizability of MAG by that of two electrically decoupled stacked monolayer graphene layers (MLG), $\Pi_q = 2\Pi_{q,\text{MLG}} = -\frac{qe^2}{2\hbar v_F}$, where $v_F \approx 10^6 \frac{\text{m}}{\text{s}}$.

By taking an inverse Fourier transform, the screened interaction of two-point charges e at distance R is obtained as

$$V(R) = e^2 \int_0^\infty dq \frac{2J_0(qR)}{1 + \kappa_{\text{hBN}} \coth qw + 2\pi\alpha}$$

Here, $J_n(x)$ is the Bessel function of the first kind and $\alpha = \frac{e^2}{\hbar v_F} \approx 2.2$. This gives a power-law falloff $V(R) \propto \frac{1}{R}$ for $R \ll w$, and $V(R)$ that decays more rapidly at distances $R > w$ (Fig. S8). The polarization charge on graphite surface due to a point charge at $r=0$ can be calculated using Gauss' law, giving by

$$G(r) = -e \int_0^\infty q dq \frac{\kappa_{\text{hBN}} J_0(qr)}{2\pi \sinh qw (1 + \kappa_{\text{hBN}} \coth qw + 2\pi\alpha)}$$

Here r is the lateral distance on the surface of graphite from the point beneath the point charge.

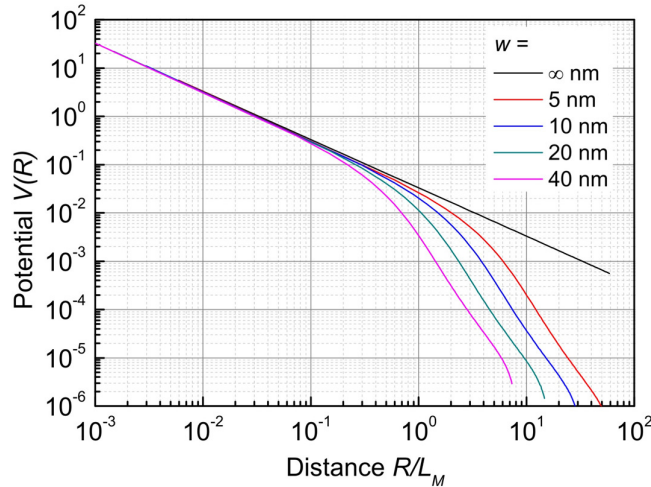


Fig. S8. **Electron-electron interaction in MAG screened by graphite substrate.** The figure shows dependence $V(R)$ versus R for several different values of the hBN spacer thickness.

Using this result, the on-site Hubbard interaction that describes the energy cost of adding an electron to the orbital that already holds one electron can now be calculated for the Wannier functions of MAG(7) as

$$U = \int_0^\infty d^2\mathbf{x} d^2\mathbf{x}' |W(\mathbf{x})|^2 |W(\mathbf{x}')|^2 V(|\mathbf{x} - \mathbf{x}'|)$$

The Wannier functions, $W(\mathbf{x})$, have a typical spatial extent of the order of L_M , the moiré lattice constant. Therefore, when the hBN thickness w is smaller than L_M , the screening effects discussed above result in a dramatic suppression of the Hubbard interaction. This behavior, as well as its impact on the MAG phase diagram, is illustrated in Fig.1A-B in the main text.

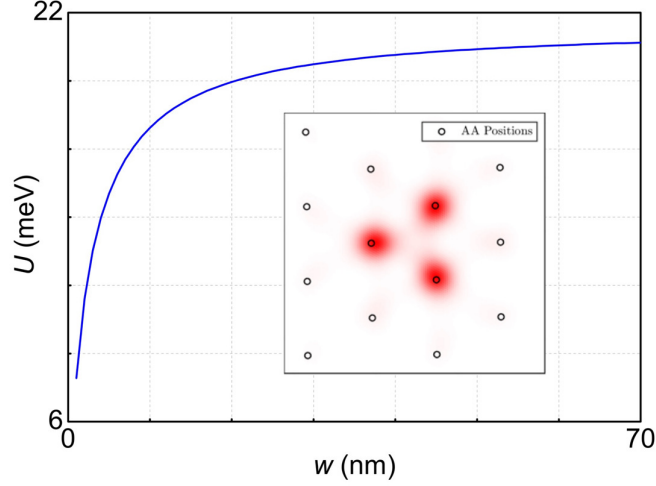


Fig. S9. Numerical calculations of Hubbard interaction dependence U versus w for realistic Wannier functions. Wannier functions are obtained for the MAG Hamiltonian using the continuum model (shown in the inset and used in Fig. 1A in the main text).

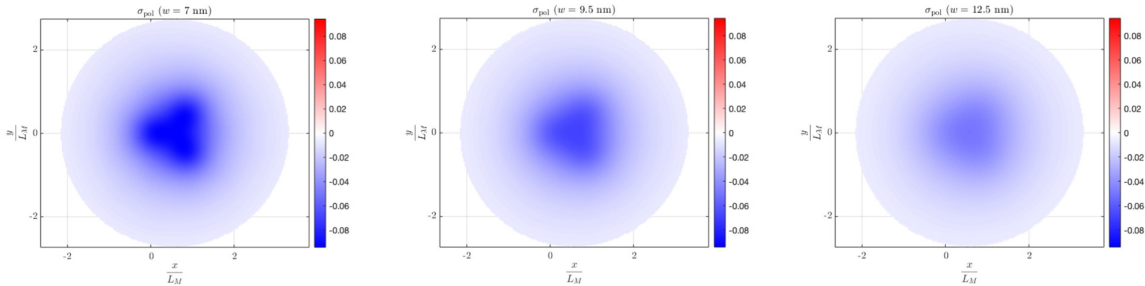


Fig. S10. Polarization charge density calculation for different thicknesses of bottom hBN spacer. L_M is Moiré superlattice period, x is the distance on the two-dimensional plane, w is the thickness of hBN spacer used for calculations. These calculations are used in Fig. 1A in the main text to demonstrate the effect of screening.

Measurement parameters.

All measurements were carried out in a dilution refrigerator at base temperatures 20 mK in out-of-plane magnetic field B . For transport measurements we employ a standard low frequency lock-in technique using Stanford Research SR860 amplifiers. For controlling back gate voltages we use Keithley 2400s voltage sourcemeters. DC voltage versus DC current measurements are performed using SR560 low-noise DC voltage preamplifier in combination with

Keithley 2700 multimeter. In order to achieve a lower electron temperature in the studied devices, we 1) perform electronic filtering of the measurement setup using a network of commercially available low-pass RC and RF filters and 2) use very low excitation currents (≤ 10 nA) due to a risk of overheating electrons and fragility of SC phases. More specific measurement parameters are given below:

Fig. 1A, 1E-F, 2, S3: Excitation current: $I_{ac} = 1$ nA; Excitation frequency: $f = 19.111$ Hz (D1 and D3), 17.333 Hz (D2); Global gate voltage: $+5$ V (D1), -8 V (D2), 0 V (D3).

Due to the increasing contact resistance at high magnetic fields we use elevated excitation current values as high as 10 nA to achieve a better signal to noise ratio in the studied samples.

Fig. 3, S4, S6: Excitation current: $I_{ac} = 10$ nA; Excitation frequency: $f = 19.111$ Hz (D1); Global gate voltage: $+5$ V (D1).

Fig. S7: Excitation frequency: $f = 19.111$ Hz (D1); Global gate voltage: $+5$ V (D1). Due to significant difference in critical currents, the SC pocket resistance in (B) was taken at excitation current $I_{ac} = 10$ nA, while the SC pocket resistance in (C) was taken at $I_{ac} = 1$ nA.

Supplementary Bibliography

1. K. Kim, A. DaSilva, S. Huang, B. Fallahazad, S. Larentis, T. Taniguchi, K. Watanabe, B. J. LeRoy, A. H. MacDonald, E. Tutuc, Tunable moiré bands and strong correlations in small-twist-angle bilayer graphene. *Proc. Natl. Acad. Sci.* **114**, 3364–3369 (2017).
2. Y. Cao, V. Fatemi, A. Demir, S. Fang, S. L. Tomarken, J. Y. Luo, J. D. Sanchez-Yamagishi, K. Watanabe, T. Taniguchi, E. Kaxiras, R. C. Ashoori, P. Jarillo-Herrero, Correlated insulator behaviour at half-filling in magic-angle graphene superlattices. *Nature*. **556**, 80–84 (2018).
3. Y. Cao, V. Fatemi, S. Fang, K. Watanabe, T. Taniguchi, E. Kaxiras, P. Jarillo-Herrero, Unconventional superconductivity in magic-angle graphene superlattices. *Nature*. **556**, 43–50 (2018).
4. X. Lu, P. Stepanov, W. Yang, M. Xie, M. A. Aamir, I. Das, C. Urgell, K. Watanabe, T. Taniguchi, G. Zhang, A. Bachtold, A. H. MacDonald, D. K. Efetov, Superconductors, Orbital Magnets, and Correlated States in Magic Angle Bilayer Graphene (2019) (available at <http://arxiv.org/abs/1903.06513>).
5. L. Wang, I. Meric, P. Y. Huang, Q. Gao, Y. Gao, H. Tran, T. Taniguchi, K. Watanabe, L. M. Campos, D. A. Muller, J. Guo, P. Kim, J. Hone, K. L. Shepard, C. R. Dean, One-dimensional electrical contact to a two-dimensional material. *Science (80-.)*. **342**, 614–617 (2013).
6. A. Uri, S. Grover, Y. Cao, J. A. Crosse, K. Bagani, D. Rodan-Legrain, Y. Myasoedov, K. Watanabe, T. Taniguchi, P. Moon, M. Koshino, P. Jarillo-Herrero, E. Zeldov, “Mapping the twist angle and unconventional Landau levels in magic angle graphene.”
7. M. Koshino, N. F. Q. Yuan, T. Koretsune, M. Ochi, K. Kuroki, L. Fu, Maximally Localized Wannier Orbitals and the Extended Hubbard Model for Twisted Bilayer Graphene. *Phys. Rev. X*. **8** (2018), doi:10.1103/PhysRevX.8.031087.